Isothermal Vapor–Liquid Equilibrium Measurements for the *n*-Pentane–Acetone System at 372.7, 397.7, and 422.6 K

Scott W. Campbell, Richard A. Wilsak, and George Thodos*

Northwestern University, Evanston, Illinois 60201

Vapor–liquid equilibrium measurements for the *n*-pentane–acetone binary have been obtained from a static high-pressure experimental facility along the 372.7, 397.7, and 422.6 K isotherms. Maximum pressure azeotropes were observed at all three temperatures. This experimental information can be represented satisfactorily by using a four-suffix Margules equation; however, the five-suffix Margules equation was required in order to correlate other related data for this system. The four parameters of this equation have been related to temperature by using the high-pressure information of this study and the subatmospheric data at 238.15, 258.15, and 298.15 K from the work of Rall and Schäfer. These correlations were used to predict accurately the isobaric work of Lo, Bieber, and Karr at atmospheric pressure. Auxiliary relationships were established which relate azeotropic pressures and compositions to temperature and indicate that azeotropic behavior extends to the critical locus consistent with the work of Kay.

Introduction

The vapor–liquid equilibrium behavior of polar–nonpolar systems presents challenges that are not encountered with nonpolar hydrocarbon systems. Systems containing both polar and nonpolar components show a higher degree of nonideality as a result of the diverse chemical nature of the components of the mixture. Such systems are ordinarily associated with the presence of azeotropes.

For this study, the *n*-pentane–acetone system has been selected for investigation. This system should produce information of a fundamental nature which should assist in the eventual prediction of vapor–liquid equilibrium behavior of polar–nonpolar systems. Experimental information available in the literature for the *n*-pentane–acetone system is limited. Vapor–liquid equilibrium measurements have been reported at 238.15, 258.15, and 298.15 K by Rall and Schäfer (*1*) and by Lo et al. (*2*) at atmospheric pressure. No experimental information exists between atmospheric pressure and the critical locus determined by Kay (*3*). The present study examines the vapor–liquid equilibrium behavior of this system at 372.7, 397.7, and 422.6 K.

Experimental Section

Materials. The *n*-pentane used in this investigation was supplied by the Phillips Petroleum Co. and was research grade with a stated purity of at least 99.84 mol %. With the exception of the degassing procedure described later, no attempt to further purify this reagent was made. The acetone used was supplied by Mallinckrodt and was of spectrophotometric grade with a stated purity of at least 99.5%, the principal impurity being water. To remove the small amount of water present in the acetone, this reagent was contacted overnight with $CaSO_4$ (Drierite). This dehydration procedure was repeated once more before decanting the acetone and subjecting it to vacuum distillation in order to remove fine suspended particles of the drying agent. A gas chromatographic analysis later indicated that this dehydration method was satisfactory. An earlier attempt to use Type 13X and Type 3A molecular sieves proved unsatisfactory because these dehydrating agents promoted reactions yielding an oily residue which remained after distilling the acetone under vacuum. Connett (*4*), as cited by Ambrose et al. (*5*), reports similar difficulties when using molecular sieves for the dehydration of acetone.

The acetone and *n*-pentane were each subjected to a degassing procedure prior to their use. This entailed freezing each reagent, evacuating the space above the solid, and then allowing them to thaw. It was found necessary to repeat this procedure three times before each of these liquids could be considered to be free of air.

Equipment. A schematic diagram of the experimental facility is shown in Figure 1 and includes, in addition to the equilibrium cell, supporting equipment for charging individual components to the cell, withdrawing samples of the liquid and vapor phases, and evacuating lines and sections.

The pressure inside the equilibrium cell was measured by using two Heise gauges: one for pressures up to 2068 kPa (300 psig) and the other for pressures up to 10 342 kPa (1500 psig). Both gauges had divisions of 1 psi and readings were estimated to 0.1 psi. The lines between these two gauges and the equilibrium cell were filled with mercury to prevent condensation of the cell contents within them. In order to establish the position of the mercury meniscus, an electrical probe was located in the line near the top of the cell. Both Heise gauges were calibrated regularly by using a dead-weight pressure balance.

Charging cells A and B were provided to store individual pure components. Each charging cell was accommodated with a mercury positive displacement pump so that the contents of these charging cells could be forced into the equilibrium cell. Scales located on each pump allowed the determination of the quantity of mercury and thus the quantity of each pure component that was displaced. Electrical probes located at the top of each charging cell ensured that no mercury was directed into the equilibrium cell.

The equilibrium cell was machined from a solid bar of 304 stainless steel and was 10.16 cm (4.00 in.) in diameter and 27.30 cm (10.75 inches) in length. A cross-sectional view of the equilibrium cell is shown in Figure 2 along with a solid insert, thrust disk, and cell cap. The contents of the equilibrium cell could be viewed through a Herculite glass window 3.175 cm thick, 2.41 cm wide, and 8.73 cm in length. This window was held in place with a hold-down bar provided with six $^1/_2$-in. bolts. Upon tightening these bolts, the window was forced against a Teflon encapsulated Silicon 70 O-ring which was imbedded in a groove surrounding the view port in the cell body. The hold-down bar and window are not shown in Figure 2.

The equilibrium chamber was machined to a diameter of 3.8 cm and was 68.7 cm^3 in volume. A seal was made between the cell body and the solid insert by using a Grafoil ribbon for a gasket. This gasket was compressed by the force transmitted through the thrust disk upon tightening eight bolts which passed through the cell cap. The solid insert was provided with

0021-9568/86/1731-0424$01.50/0

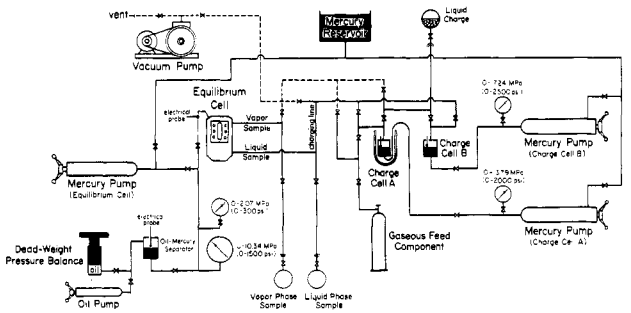

Figure 1. Schematic diagram of experimental facility.

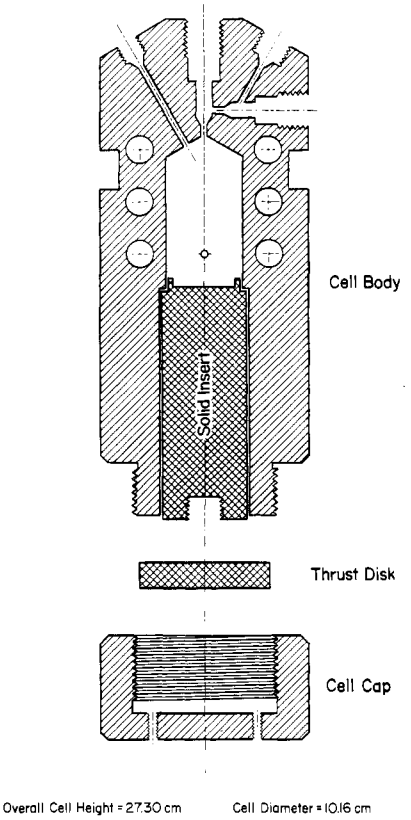

Figure 2. Cross-sectional view of vapor–liquid equilibrium cell.

a threaded hole at its base to allow for its removal. The opening at the upper left of Figure 2 connects to the pressure measurement system. The vertical opening at the top of Figure 2 contains the vapor trap valve while the horizontal opening to the right accommodates the vapor release valve. Before a vapor sample was trapped, the space between these two valves was evacuated. The vapor release valve was then closed and the vapor trap valve was momentarily opened to trap a sample of the vapor phase. The vapor release valve was then opened and the sample expanded through the right oblique opening to the vapor sample bulb. A similar arrangement of valves, not shown in Figure 2, was provided to sample the liquid phase.

A magnetic stirrer was used to ensure intimate contact between the vapor and liquid phases. A pair of electromagnets was situated externally within the grooved top of the cell body. Upon energizing these magnets, a soft iron ring resting on top of the solid insert jumped to the top of the equilibrium chamber. In order to minimize secondary thermal effects, these magnets were energized 1 s out of every 30 s by using a switching timer.

The equilibrium cell was surrounded by two concentric cubical air baths, the walls of which were constructed from Maranite insulation. Each air bath was provided with electrical plate heaters. The heaters of the outer bath were controlled manually with autotransformers, while those in the inner bath were controlled with a proportionating temperature controller (Omega Engineering, Model 49).

The temperature of the equilibrium cell was measured with three copper–constantan thermocouples which were placed in thermowells drilled into the cell body. The thermocouples were calibrated on the IPTS-68 by using the ice point of water, the boiling point of water, and the melting point of tin as fixed points. The estimated accuracy of the temperature measurements is 0.1 K with a precision of 0.04 K.

Compositions of the liquid and vapor phases were determined by using a gas chromatograph (Beckman Instruments, Model GC 72–5) with a recorder and a disk integrator. The gas chromatograph was calibrated by using mixtures of known composition which were prepared in a separate gas mixing facility. Three chromatograms were obtained for each sample, and the resulting compositions were averaged. These compositions have an estimated precision of 0.005 mole fraction.

Procedure. After the equilibrium cell was brought to temperature it was evacuated along with the lines between it and the charging cells. One of the pure components was charged to the equilibrium cell and its vapor pressure was measured. A measured amount of the other component was then added to the equilibrium cell. After equilibrium was attained, the pressure was recorded and the liquid and vapor phases were sampled. These samples were frozen into their respective sample bulbs by using liquid nitrogen and were then transferred to the mixing facility. After each sample was thawed and vaporized, helium was introduced until the pressure in each bulb was above atmospheric. Measured amounts of each sample were then injected into the gas chromatograph with a 1-mL gas-tight syringe.

After the compositions of both the vapor and liquid samples were established, a measured amount of the second component was added to the equilibrium cell to prepare it for the next measurement. When approximately one-half of the isotherm was covered in this manner, the equilibrium cell was emptied and refilled with the other pure component and the process was repeated for the other half of the isotherm.

Results and Discussion

Experimental Results. The compositions of the vapor and liquid phases as well as the equilibrium pressures were measured for the 372.7, 397.7, and 422.6 K isotherms. These measurements are presented in Table I and are shown in Figure 3. These plots indicate the existence of maximum pressure azeotropes at all three temperatures. Van Ness et al. (*6*) discuss the importance of measuring pure component vapor pressures using the same materials and equipment as used in obtaining the vapor–liquid equilibrium data. Therefore, the pure component vapor pressures of the *n*-pentane and acetone used in this study were measured at each of the above temperatures. These values are also included in Table I and Figure 3.

Treatment of Data. A thermodynamic treatment of the vapor–liquid equilibrium data requires that, in addition to temperature and pressure, the fugacity of each component be the same in both phases. Thus, for component *i*

$$f_i^{v} = f_i^{l} \tag{1}$$

Vapor-phase fugacities have been calculated by using the pressure-explicit virial equation of state, truncated after the second term

$$\frac{PV}{RT} = 1 + \frac{B}{V} \tag{2}$$

Table I. Vapor–Liquid Equilibrium Measurements and Calculated Values and Activity Coefficients for the *n*-Pentane (1)–Acetone (2) System at 372.7, 397.7, and 422.6 K

	mole fraction				calculated	
P, kPa	x_1	y_1	$\ln \gamma_1$	$\ln \gamma_2$	P, kPa	y_1
			T = 372.7 K			
366.1	0.000	0.000				
478.1	0.084	0.265	1.023	0.015	477.3	0.267
551.6	0.180	0.374	0.719	0.090	552.7	0.403
613.3	0.315	0.510	0.544	0.124	613.2	0.508
642.2	0.422	0.546	0.355	0.260	642.1	0.566
660.9	0.532	0.616	0.260	0.336	661.0	0.618
672.2	0.649	0.671	0.156	0.492	671.2	0.674
668.1	0.785	0.753	0.070	0.705	668.4	0.749
637.8	0.916	0.869	0.016	0.995	638.5	0.864
587.4	1.000	1.000				
			T = 397.7 K			
669.5	0.000	0.000				
760.1	0.044	0.135	0.997	0.003	756.0	0.132
820.8	0.087	0.208	0.801	0.024	825.4	0.224
886.0	0.133	0.294	0.772	0.024	886.4	0.297
968.0	0.210	0.392	0.659	0.042	965.0	0.386
1047.0	0.331	0.478	0.449	0.124	1047.7	0.482
1083.9	0.412	0.533	0.356	0.175	1084.4	0.532
1109.7	0.495	0.569	0.250	0.271	1110.8	0.578
1128.0	0.576	0.621	0.190	0.339	1127.2	0.621
1134.9	0.702	0.701	0.109	0.478	1134.7	0.693
1114.5	0.824	0.790	0.048	0.660	1114.3	0.780
1067.6	0.919	0.882	0.014	0.851	1067.7	0.877
991.8	1.000	1.000				
			T = 422.6 K			
1125.2	0.000	0.000				
1362.4	0.114	0.208	0.617	0.027	1369.1	0.224
1481.0	0.180	0.298	0.561	0.045	1478.4	0.311
1586.8	0.257	0.381	0.480	0.070	1580.7	0.390
1739.2	0.445	0.537	0.296	0.156	1740.3	0.529
1798.5	0.658	0.663	0.109	0.379	1805.2	0.661
1781.9	0.794	0.770	0.050	0.539	1778.0	0.762
1722.3	0.879	0.847	0.020	0.671	1721.2	0.842
1635.8	0.956	0.931	−0.001	0.881	1634.2	0.934
1566.1	1.000	1.000				

where the second virial coefficient of the mixture is $B = \sum_i \sum_j B_{ij} y_i y_j$. Using eq 2, it can be shown that the vapor-phase fugacity of component i is given by

$$f_i^{v} = P y_i \exp\left[\frac{2\sum_j B_{ij} y_j}{V} - \ln \frac{PV}{RT}\right] \quad (3)$$

The liquid-phase fugacity of component i can be expressed in terms of the activity coefficient, γ_i, and the standard-state fugacity, f_i°, as

$$f_i^{l} = \gamma_i x_i f_i^{\circ} \quad (4)$$

If the standard-state fugacity of component i is chosen to be the fugacity of pure component i in the liquid state at the same temperature and pressure of the mixture, the standard-state fugacity becomes

$$f_i^{\circ} = P_i^{sat} \exp\left[\frac{2B_{ii}}{V_i^{v}} - \ln \frac{P_i^{sat} V_i^{v}}{RT} + \frac{(P - P_i^{sat}) V_i^{l}}{RT}\right] \quad (5)$$

where eq 2 was used to integrate up to P_i^{sat}, the vapor pressure of pure component i, and V_i^{l} was assumed constant and equal to the saturated liquid volume in the Poynting correction term.

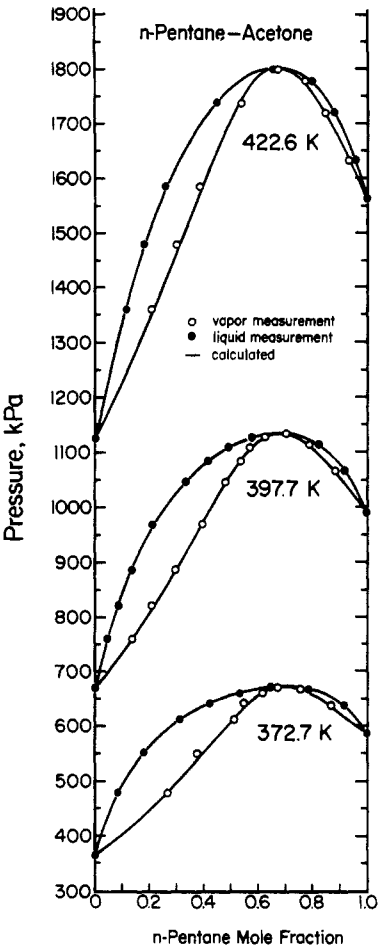

Figure 3. Vapor–liquid equilibrium behavior for the *n*-pentane–acetone system at 372.7, 397.7, and 422.6 K.

Table II. Second Virial Coefficients (cm³/mol) and Saturated Liquid Volumes (cm³/mol) for the *n*-Pentane (1)–Acetone (2) System

T, K	B_{11}	B_{12}	B_{22}	V_1^{l}	V_2^{l}
372.7	−692.8	−529.0	−854.2	134.4	83.8
397.7	−593.5	−452.6	−692.9	143.6	88.3
422.6	−514.5	−391.3	−575.3	156.5	94.0

Combining eq 1 and 3–5 yields an expression for the activity coefficient

$$\gamma_i = \frac{P y_i}{P_i^{sat} x_i} \frac{\exp\left[\frac{2\sum_j B_{ij} y_j}{V} - \ln \frac{PV}{RT}\right]}{\exp\left[\frac{2B_{ii}}{V_i^{v}} - \ln \frac{P_i^{sat} V_i^{v}}{RT} + \frac{(P - P_i^{sat}) V_i^{l}}{RT}\right]} \quad (6)$$

Values for the second virial coefficient were obtained from the correlation given by Tsonopoulos (*7*) with k_{ij} taken as 0.10. These values are in agreement with those compiled by Dymond and Smith (*8*) for pure *n*-pentane and pure acetone. Values for the saturated liquid volumes were calculated by using the actual density parameters given by Campbell and Thodos (*9*). The resulting values of the second virial coefficients and saturated liquid volumes are presented in Table II.

Activity coefficients have been calculated for each of the experimental measurements by using eq 6 and are given in

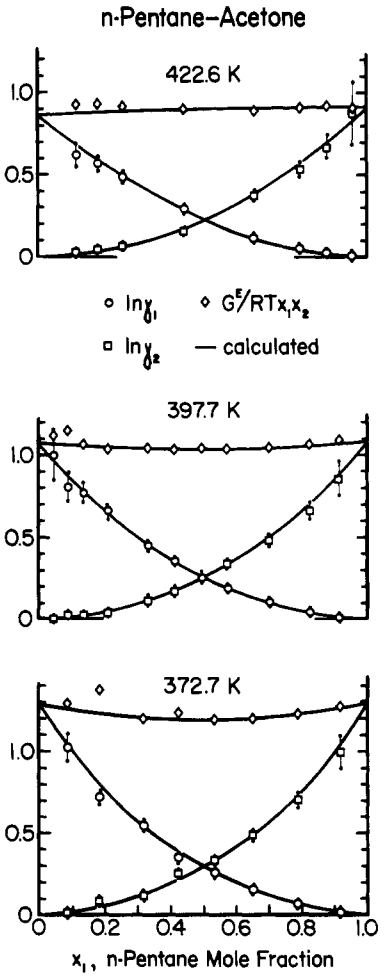

Figure 4. Activity coefficients and excess Gibbs free energies for the *n*-pentane–acetone system at 372.7, 397.7, and 422.6 K.

Table I and shown in Figure 4. These values have been used to calculate the excess Gibbs free energy from the relationship

$$\frac{G^E}{RT} = \sum_i x_i \ln \gamma_i \tag{7}$$

The excess Gibbs free energy divided by the product of the liquid-phase mole fractions is also shown in Figure 4. If this ratio related linearly to x_1, the three-suffix Margules equation would apply. However, if G^E/RTx_1x_2 vs. x_1 is not linear, a higher order Margules equation is required. The simplest extension of the three-suffix Margules equation is the four-suffix Margules equation

$$\frac{G^E}{RT} = x_1x_2[\alpha x_2 + \beta x_1 - \delta x_1x_2] \tag{8}$$

The expressions for the activity coefficients corresponding to eq 8 become

$$\ln \gamma_1 = x_2^2[\alpha + 2(\beta - \alpha - \delta)x_1 + 3\delta x_1^2] \tag{9}$$

$$\ln \gamma_2 = x_1^2[\beta + 2(\alpha - \beta - \delta)x_2 + 3\delta x_2^2] \tag{10}$$

Although values of α, β, and δ could be obtained from Table I by a least-squares fit of G^E/RTx_1x_2 to x_1, the approach outlined by Barker (*10*) using only P–x data was adopted. This approach has been examined by Abbott and Van Ness (*11*) who found that the use of vapor-phase mole fractions in the data reduction process can lead to distortions in the correlation of the excess Gibbs free energy. Although the basic idea of Barker's method was retained in the present study, the optimal values of α, β, and δ were obtained by using a nonlinear regression routine rather than the suggested numerical approach.

Table III. Values of Parameters for Eq 8 Resulting from Barker's Method as well as Overall Root Mean Square Deviations in y_1 and P

				root mean square deviations	
T, K	α	β	δ	Δy_1	ΔP, kPa
372.7	1.2833	1.2936	0.4166	0.013	0.7
397.7	1.0763	1.0842	0.1826	0.007	2.1
422.6	0.8628	0.9130	−0.0418	0.009	4.4

Values for parameters α, β, and δ as well as the resulting overall root mean square deviations in y_1 and P are given in Table III. Calculated values of y_1 and P corresponding to each measured liquid composition are given in Table I.

Included in Figure 4 are predicted curves for $\ln \gamma_1$, $\ln \gamma_2$ and G^E/RTx_1x_2 from the values of α, β, and δ obtained from the nonlinear regression analysis. Since eq 9 and 10 satisfy the isobaric–isothermal form of the Gibbs–Duhem equation, the curves drawn in Figure 4 are thermodynamically consistent on the assumption that the effect of pressure on the activity coefficients may be neglected. This assumption has been made throughout this study. An indication that the experimental measurements are thermodynamically consistent follows from the degree to which they conform to the curves for $\ln \gamma_1$ and $\ln \gamma_2$ shown in Figure 4. In this regard, error bars are shown in this figure and were calculated by using estimated uncertainties in both composition (0.005) and pressure (0.1 psi). The effect of uncertainty in temperature was not taken into account. The fact that only two of the error bars on the 372.7 K isotherm failed to intersect the predicted curves lends credence to the contention that the data are thermodynamically consistent.

Temperature Dependence of the Excess Gibbs Free Energy. Isothermal vapor–liquid equilibrium data at 238.15, 258.15, and 298.15 K are reported by Rall and Schäfer (*1*). In addition, excess enthalpy data at 243.2, 253.2, 273.2, and 293.2 are reported by Schäfer and Rohr (*12*) as referenced by Schäfer (*13*).

The Gibbs–Helmholtz equation

$$\left[\frac{\partial(G^E/RT)}{\partial T}\right]_{P,x} = -\frac{H^E}{RT^2} \tag{11}$$

provides a relationship between the excess Gibbs free energy and excess enthalpy. If a Margules-type equation is used to model liquid-phase nonidealities, the excess Gibbs free energy and the excess enthalpy have the same functional dependence on composition. Although it was found that the four-suffix Margules equation was adequate for describing the vapor–liquid equilibrium behavior of the data of this study as well as those of Rall and Schäfer (*1*), a five-suffix Margules equation was required to represent the excess enthalpy data of Schäfer and Rohr (*12*). In order to present a generalized description of the temperature dependence of the excess Gibbs free energy, all available data for this system were treated by using the five-suffix Margules equation

$$\frac{G^E}{RT} = x_1x_2[\alpha x_2 + \beta x_1 - (\epsilon x_2 + \kappa x_1)x_1x_2] \tag{12}$$

where α, β, ϵ, and κ are assumed to be independent of pressure and thus depend only on temperature. The expressions for the activity coefficients corresponding to eq 12 become

$$\ln \gamma_1 = x_2^2[\alpha + 2(\beta - \alpha)x_1 + 2(\kappa x_1 + \epsilon x_2)x_1(x_1 - x_2) - \kappa x_1^2] \tag{13}$$

$$\ln \gamma_2 = x_1^2[\beta + 2(\alpha - \beta)x_2 + 2(\kappa x_1 + \epsilon x_2)x_2(x_2 - x_1) - \epsilon x_2^2] \tag{14}$$

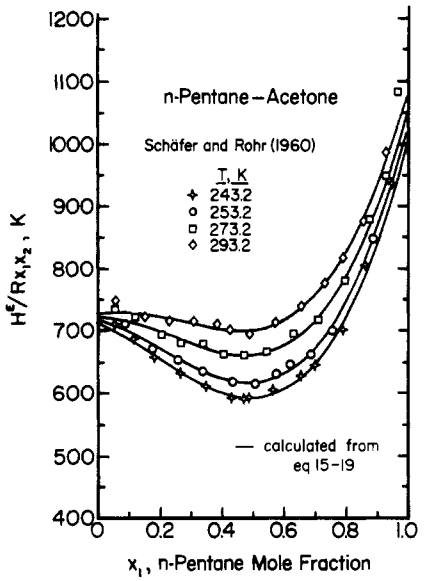

Figure 5. Correlation of excess enthalpy data of Schäfer and Rohr using the five-suffix Margules equation.

Using eq 11, we obtain the corresponding expression for the excess enthalpy

$$\frac{H^E}{R} = x_1x_2[Ax_2 + Bx_1 - (Cx_2 + Dx_1)x_1x_2] \quad (15)$$

where $A = -T^2(d\alpha/dT)$, $B = -T^2(d\beta/dT)$, $C = -T^2(d\epsilon/dT)$, and $D = -T^2(d\kappa/dT)$.

Assuming that a linear reciprocal temperature dependence for A, B, C, and D exists, the excess enthalpy data were correlated with temperature to give the following expressions:

$$A = 789.2 - 18932/T \quad (16)$$

$$B = 1471.0 - 112230/T \quad (17)$$

$$C = -1069.8 + 384870/T \quad (18)$$

$$D = 213.7 + 348000/T \quad (19)$$

Figure 5 shows a comparison between the excess enthalpy data of Schäfer and Rohr (*12*) and the correlation given by eq 15–19. Table IV shows root mean square and average percent deviations in H^E resulting from this comparison.

Equations 16–19 specify α, β, ϵ, and κ within a constant of integration. These integration constants were selected to obtain the best possible agreement to the values of α, β, ϵ, and κ obtained from all of the isothermal vapor–liquid equilibrium data. Upon integration of eq 16–19 according to the definitions of A, B, C, and D, and addition of the integration constants, the following relationships result:

$$\alpha = -0.778 + \frac{789.2}{T} - \frac{9466}{T^2} \quad (20)$$

$$\beta = -2.251 + \frac{1471.0}{T} - \frac{56115}{T^2} \quad (21)$$

$$\epsilon = 1.836 - \frac{1069.8}{T} + \frac{192435}{T^2} \quad (22)$$

$$\kappa = -1.448 + \frac{213.7}{T} + \frac{174000}{T^2} \quad (23)$$

Figure 6 shows a comparison between experimentally determined activity coefficients and those calculated by using eq 13 and 14 and eq 20–23. In addition, Table IV shows root mean square deviations in pressure and vapor-phase composition between experimental measurements and those resulting from the use of eq 13 and 14 and eq 20–23. This table also includes the resulting overall average percent deviations in pressure.

Table IV. Root Mean Square (rms) and Average Percent Deviations for Isothermal Excess Enthalpy and Vapor–Liquid Equilibrium Data and Vapor–Liquid Equilibrium Data at Atmosphere Pressure for the *n*-Pentane–Acetone System

Isothermal Excess Enthalpy, H^E

		deviations	
	T, K	rms, kJ	av %
Schäfer and Rohr (*10*)	243.2	8.1	0.81
	253.2	10.2	1.04
	273.2	9.1	1.21
	293.2	7.5	0.72

Isothermal Vapor–Liquid Equilibrium

			ΔP	
	T, K	rms Δy_1	rms, kPa	av %
Rall and Schäfer (*1*)	238.15	0.0102	0.077	1.35
	258.15	0.0069	0.153	1.04
	298.15	0.0030	0.58	0.73
this investigation	372.7	0.013	1.2	0.19
	397.7	0.009	6.5	0.59
	422.6	0.012	21.6	1.12

Isobaric Vapor–Liquid Equilibrium

			ΔT	
	P, kPa	rms Δy_1	rms, K	av %
Lo, Bieber, and Karr (*2*)	101.325	0.016	0.78	0.11

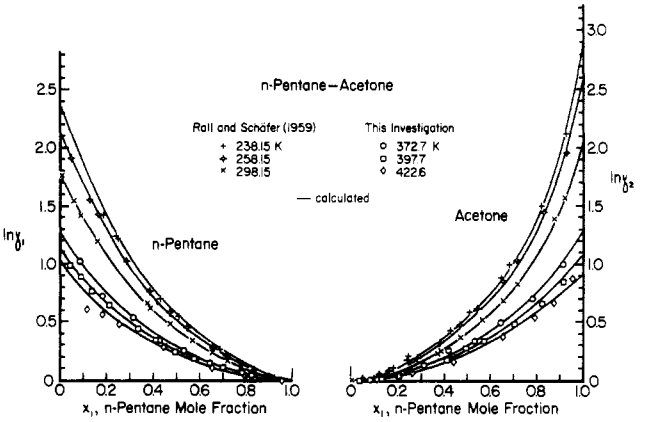

Figure 6. Comparison between activity coefficients obtained from experimental measurements and those calculated by using eq 13 and 14 and eq 20–23.

An independent check of the validity of eq 20–23 is given by their application to a set of isobaric vapor–liquid equilibrium data not used in their development. In this regard, these equations have been applied to the atmospheric pressure data of Lo et al. (*2*) to calculate temperature and vapor-phase composition given the pressure and liquid-phase composition. The calculated vapor–liquid equilibrium behavior as well as the experimental measurements are shown in Figure 7 and resulting deviations in temperature and vapor-phase composition are given in Table IV. The pure component boiling temperatures for both acetone and *n*-pentane measured by Lo et al. are also shown in Figure 7. These measurements, along with the predicted curves, indicate that the point at 322.53 K might be in error.

In these calculations, it was also necessary to express saturated liquid volumes, second virial coefficients, and vapor pressures as functions of temperature. The saturated liquid volumes were obtained by using the correlation of Campbell and Thodos (*9*) while the correlation of Tsonopoulos (*7*) was used

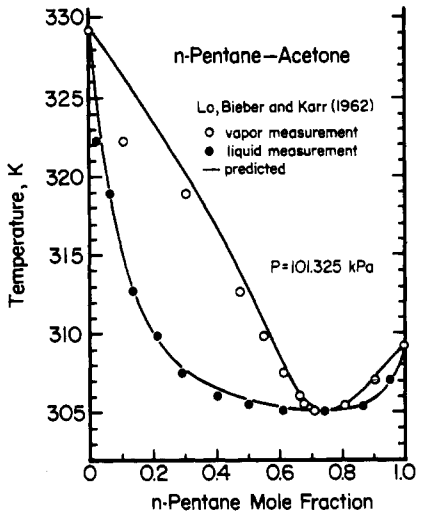

Figure 7. Comparison between vapor–liquid equilibrium measurements at atmospheric pressure and those predicted by using eq 13 and 14 and eq 20–23.

Table V. Azeotropic Behavior of the *n*-Pentane–Acetone System

	from exptl data		use of eq 13, 14, 20–23		calculated	
T, K	z_1	P^{azeo}, kPa	z_1	P^{azeo}, kPa	z_1[a]	P^{azeo}, kPa
			Rall and Schäfer (*1*)			
238.15	0.794	4.28	0.805	4.33	0.794	4.30
258.15	0.777	13.72	0.792	13.60	0.778	13.56
298.15	0.749	77.8	0.754	77.2	0.748	78.8
			Lo, Bieber, and Karr (*2*)			
305.01	0.742	101.3	0.746	101.2	0.743	100.9
			This Investigation			
372.7	0.701	672	0.697	673	0.700	671
397.7	0.684	1136	0.675	1140	0.687	1134
422.6	0.676	1799	0.659	1819	0.675	1802

[a] From eq 24. [b] From eq 25.

to obtain the second virial coefficients. Pure component vapor pressures were obtained from the correlation of Gómez-Nieto and Thodos using the tabulated actual vapor pressure parameters for acetone (*14*) and *n*-pentane (*15*).

Azeotropic Behavior. The data of Rall and Schäfer (*1*) for the *n*-pentane–acetone system indicate that maximum pressure azeotropic behavior exists for temperatures as low as 238.15 K. Furthermore, Kay (*3*) showed from critical temperature and pressure measurements that this behavior extended to the critical locus, but did not have sufficient information to locate the critical azeotropic composition. The data of this study, shown in Figure 3, provide a means of extending the results of Rall and Schäfer to the critical locus. From the experimental data of this study and those of Rall and Schäfer, a plot of $y_1 - x_1$ vs. x_1 was constructed and values of the azeotropic composition were read at the point where $y_1 - x_1 = 0$. Azeotropic pressures were then read from the plots of P vs. x_1 at these compositions. These values obtained from experimental data are given in Table V, along with the azeotrope at atmospheric pressure reported by Lo et al. (*2*). Also included in Table V are the azeotropic pressures and compositions predicted by using the correlation for the activity coefficients given by eq 13 and 14 and eq 20–23. When compared with values obtained from experimental data, these calculated results show an average deviation of 0.009 in z_1, the azeotropic composition, and an average percent deviation of 0.65 for the azeotropic pressure.

Since the establishment of azeotropic compositions and pressures from the correlation of activity coefficients involves a trial-and-error procedure, it proves more expedient to develop empirical relationships for their dependence on temperature. From the values obtained from the experimental data of Rall and Schäfer (*1*) and Lo et al. (*2*) and those of this study, the following relationship for the azeotropic composition was developed:

$$z_1 = 1.0505 - 1.3197 \times 10^{-3}T + 1.0181 \times 10^{-6}T^2 \quad (24)$$

Figure 8 shows the critical temperature–composition behavior for the *n*-pentane–acetone system resulting from the data of Kay (*3*) and also the azeotropic compositions used to establish eq 24. The intersection of eq 24 with the critical temperature curve is $z_1^c = 0.656$ and $T_c^{azeo} = 468.2$ K. The critical composition is in slight disagreement with the statement made by Kay (*3*) that this value be $0.54 \leq z_1^c \leq 0.63$. The pressure of the critical azeotrope corresponding to $z_1^c = 0.656$ was found from the critical pressure–composition behavior given by Kay to be $P_c^{azeo} = 3760$ kPa.

A plot of azeotropic pressure vs. reciprocal temperature on semilogarithmic coordinates for the values resulting from the available data is shown in Figure 9. This figure also includes the critical locus of this system as well as the vapor pressures of the pure components calculated from the actual vapor pressure parameters given by Gómez-Nieto and Thodos. This figure suggests that the azeotropic pressures relate to temperature in the same manner as that of the pure components. Thus, a vapor pressure equation of the form suggested by Gómez-Nieto and Thodos (*14*) was adopted to represent the

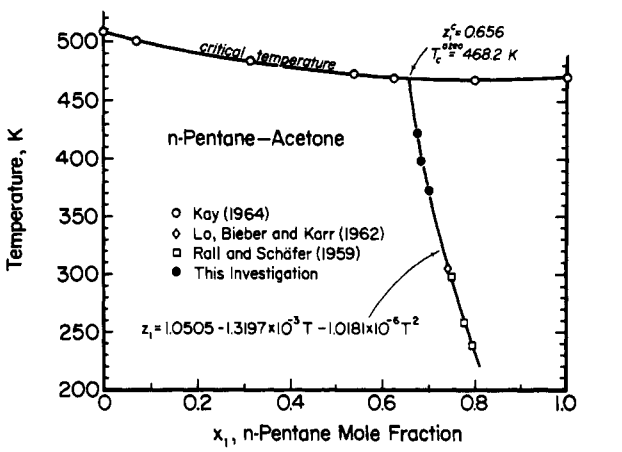

Figure 8. Relationship between azeotropic composition and temperature and its intersection with the critical temperature line.

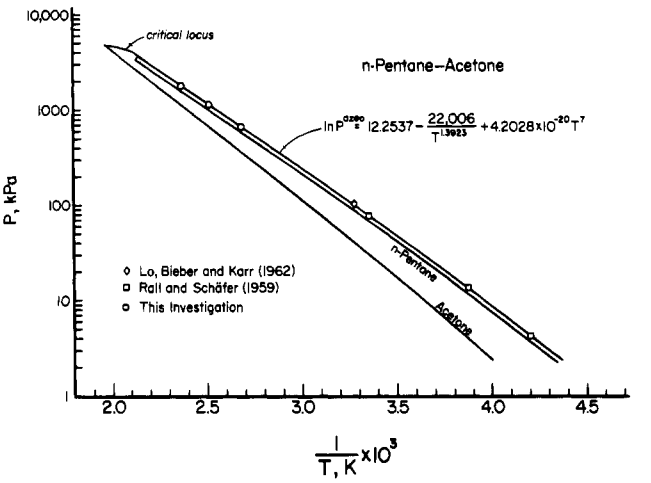

Figure 9. Dependence of azeotropic pressure on temperature for the *n*-pentane–acetone system.

dependence of azeotropic pressure on temperature as

$$\ln P^{azeo}(kPa) = 12.2537 - \frac{22066}{T^{1.3923}} + 4.2028 \times 10^{-20} T^7 \quad (25)$$

which yields for the critical point, $P_c^{azeo} = 3780$ kPa at $T_c^{azeo} = 468.2$ K. Values for the azeotropic compositions and azeotropic pressures calculated from eq 24 and 25, respectively, are included in Table V. When compared with values obtained from experimental data, the calculated values show an average deviation of 0.001 in z_1 and an average percent deviation of 0.56 for P^{azeo}.

Glossary

A, B, C, D	temperature-dependent parameters, K (eq 15)
B	second virial coefficient, cm^3/mol
f	fugacity, kPa
G	Gibbs free energy, J/mol
H	enthalpy, J/mol
k_{ij}	binary interaction coefficient in Tsonopoulos correlation
P	pressure, kPa
R	gas constant
T	absolute temperature, K
V	molar volume, cm^3/mol
x	liquid mole fraction
y	vapor mole fraction
z	azeotropic composition, mole fraction

Greek Letters

α, β, δ	parameters (eq 8)
α, β, ϵ, κ	temperature-dependent parameters (eq 12)
γ	activity coefficient

Superscripts

azeo	azeotropic state
c	critical state
E	excess property
l	liquid state for pure component or mixture
sat	saturated state
v	vapor state for pure component or mixture
°	standard state

Subscripts

c	critical state
i	component *i*
j	component *j*
1	*n*-pentane
2	acetone

Registry No. Pentane, 109-66-0; acetone, 67-64-1.

Literature Cited

(1) Rall, W.; Schäfer, K. *Z. Elektrochem.* **1959**, *63*, 1019.
(2) Lo, T. C.; Bieber, H. H.; Karr, A. E. *J. Chem. Eng. Data* **1962**, *7*, 327.
(3) Kay, W. B. *J. Phys. Chem.* **1964**, *68*, 827.
(4) Connett, J. E. *Lab. Pract.* **1972**, *21*, 545.
(5) Ambrose, D.; Sprake, C. H. S.; Townsend, R. *J. Chem. Thermodyn.* **1974**, *6*, 693.
(6) Van Ness, H. C.; Byer, S. M.; Gibbs, R. E. *AIChE J.* **1973**, *19*, 238.
(7) Tsonopoulos, C. *AIChE J.* **1974**, *20*, 263.
(8) Dymond, J. H.; Smith, E. B., *The Virial Coefficients of Pure Gases and Mixtures: A Critical Compilation*; Clarendon Press: Oxford, V.K., 1980.
(9) Campbell, S. W.; Thodos, G. *Ind. Eng. Chem. Fundam.* **1984**, *23*, 500.
(10) Barker, J. A.; Austr. *J. Chem.* **1953**, *6*, 207.
(11) Abbott, M. M.; Van Ness, H. C. *AIChE J.* **1975**, *21*, 62.
(12) Schäfer, K.; Rohr, F. J. *Z. Phys. Chem. NF* **1960**, *24*, 130.
(13) Schäfer, K. *Int. DATA Ser., Sel. Data Mixtures, Ser. A.* **1978**(1), 76.
(14) Gómez-Nieto, M. A.; Thodos, G. *Can. J. Chem. Eng.* **1977**, *55*, 445.
(15) Gómez-Nieto, M. A.; Thodos, G. *Ind. Eng. Chem. Fundam.* **1978**, *17*, 45.

Received for review February 14, 1986. Accepted May 22, 1986. We extend our gratitude for the partial financial support granted by the National Science Foundation through Grant CPE-7920434 and also to the Exxon Education Foundation for the financial support of S.W.C.

Tetramethylammonium Perchlorate: Ion Size Parameters in Solution and in the Solid State

Patience C. Ho* and J. B. Ramsey†

Chemistry Division, Oak Ridge National Laboratory, Oak Ridge, Tennessee 37831

The association constants at 25 °C of tetramethylammonium perchlorate in pyridine, 2-butanone, acetone, benzonitrile, and nitrobenzene have been determined. It is shown that the association constants (K_A) conform to a straight-line relation between ln K_A and $1/D$ as predicted by the Denison–Ramsey theory of ion-pair formation. The a parameter, the distance between ions in the ion pair, of this salt determined from the slope of this straight line ($a = e^2/kT \times$ slope) is found to be 7.3 ± 0.1 Å, considerably larger than the N–Cl distance in its crystal.

†This paper is dedicated to the memory of Professor J. B. Ramsey (1892–1965).

Introduction

Before 1955 the most widely used relation between the dissociation constant of a salt in any solvent with sufficiently low dielectric constant, the temperature, the dielectric constant of solvents, and the interionic distance in associated ion pairs was developed by Bjerrum (*1*). However, the Bjerrum theory has certain inherent mathematical and physical defects (*2*). Denison and Ramsey (*3*) proposed a basis for counting associated ion pairs (only ions in contact are counted as ion pairs). From a thermodynamic consideration of a stepwise process for bringing about the change from an associated ion pair of a uni-univalent salt (in which the interionic distance has been called the "contact distance" and designated the a parameter) to the two free ions with interionic distance sufficiently large to permit the intervention of solvent molecules, an equation

0021-9568/86/1731-0430$01.50/0